vibration

MDPI

Article

Frequency-Dependent Vibration Damping and Energy Dissipation in Monolayer and Bilayer Graphene: A Molecular Dynamics Study

Antonios V. Iliopoulos and Georgios I. Giannopoulos *

Department of Mechanical Engineering, School of Engineering, University of the Peloponnese, 26334 Patras, Greece; ant.iliopoulos@uop.gr
* Correspondence: ggiannopoulos@uop.gr

Abstract

The vibration damping behavior of monolayer and bilayer graphene is investigated through molecular dynamics simulations, with particular emphasis on the effects of excitation frequency and interlayer interactions on mechanical energy dissipation. Graphene nanoplates with in-plane dimensions of approximately 200 Å × 200 Å are considered, with the bilayer system arranged in an AB-stacking configuration. Atomic interactions are described using a reactive force field (ReaxFF), enabling the dynamic response and associated energy dissipation to emerge directly from the underlying atomistic interactions without introducing phenomenological damping parameters. A localized harmonic out-of-plane displacement with an amplitude of 0.4 nm is applied to the central region of the graphene nanoplate at excitation frequencies of 0.001, 0.01, 0.1, and 1 THz. Energy dissipation is quantified directly from the area enclosed by the resulting reaction force–displacement hysteresis loops, providing an energy-based characterization of the equivalent damping response. The results reveal a strongly frequency-dependent damping response and a non-monotonic effect of the second graphene layer. At 1 THz, the equivalent damping ratio reaches approximately 47.4% for monolayer graphene and 24.0% for bilayer graphene, despite comparable absolute cycle-energy values, demonstrating that the normalized damping response is strongly influenced by the dynamic reference energy. Overall, the results show that interlayer coupling can substantially modify the frequency-dependent vibration and energy-dissipation response of graphene rather than producing a uniform increase in damping.

Keywords: monolayer graphene; bilayer graphene; vibration damping; energy dissipation; molecular dynamics; ReaxFF; hysteresis; equivalent damping ratio

Check for updates

Academic Editors: Aleksandar Pavic, Mohamed Hamdaoui, Kouider Bendine, George Papagiannopoulos and Saeed Bab

Received: 14 September 2026
Revised: 4 October 2026
Accepted: 12 October 2026
Published: 15 October 2026

Copyright: © 2026 by the authors. Licensee MDPI, Basel, Switzerland. This article is an open access article distributed under the terms and conditions of the Creative Commons Attribution (CC BY) license.

1. Introduction

Graphene has attracted sustained scientific and technological interest since its experimental isolation, owing to its exceptional combination of mechanical, electrical, and thermal properties [1,2]. Its two-dimensional honeycomb lattice, composed of strongly bonded sp^2 carbon atoms, provides remarkably high in-plane stiffness and strength while retaining an extremely low areal mass density [3]. These characteristics make graphene particularly attractive for nanoelectromechanical systems (NEMS), where low mass, high stiffness, and large surface-to-volume ratio enable resonators, oscillators, sensors, and other devices capable of operating at very high frequencies [4–6]. In such applications,

however, high resonant performance alone is not sufficient. The mechanisms governing vibration attenuation and mechanical energy dissipation are equally important, since they directly influence the quality factor, resonance bandwidth, dynamic stability, sensitivity, and transient response of graphene-based nanodevices.

The vibration and damping characteristics of graphene have therefore been investigated using both experimental and theoretical approaches. Measurements on graphene mechanical resonators have demonstrated that their energy dissipation depends strongly on temperature, geometry, edge configuration, boundary conditions, and operating conditions [7,8]. At the nanoscale, the physical origins of damping differ substantially from the phenomenological mechanisms commonly employed to represent dissipation in continuum-scale structural dynamics. In pristine graphene, mechanical energy can be redistributed through anharmonic lattice interactions, coupling among vibrational modes, phonon-mediated processes, edge effects, and nonlinear interactions between flexural and in-plane motion. Consequently, the effective damping response of graphene cannot necessarily be represented by a single frequency- and amplitude-independent material parameter.

Nonlinearity is particularly important in the dynamic response of graphene resonators. Eichler et al. experimentally demonstrated pronounced nonlinear damping in resonators based on carbon nanotubes and graphene [9], while Croy et al. theoretically related linear and nonlinear damping in graphene resonators to the coupling between flexural motion and in-plane phonons [10]. Keşkekler et al. subsequently showed that nonlinear damping can be tuned through parametric-direct internal resonance, highlighting the strong coupling between different vibration modes in graphene nanoresonators [11]. Atomistic simulations have provided complementary information that is difficult to obtain experimentally. Kunal and Aluru investigated phonon-mediated losses in graphene nanoribbons [12], whereas Jiang and Wang demonstrated through molecular dynamics (MD) simulations that the vibration characteristics of graphene-based torsional resonators emerge directly from their atomistic dynamics [13]. These findings collectively indicate that graphene damping is intrinsically connected to the dynamic state of the lattice and can exhibit a strong dependence on excitation conditions.

An additional level of complexity arises when a second graphene layer is introduced. Whereas the dynamic response of monolayer graphene is governed primarily by intralayer covalent interactions and the associated lattice dynamics, bilayer and multilayer graphene introduce interlayer interactions and relative motion between adjacent sheets. Experimental measurements by Lahiri et al. revealed a pronounced layer-dependent damping response in multilayer graphene membranes under low-frequency cyclic loading [14]. Atomistic simulations by Kim and Park further demonstrated that multilayer friction and attachment can significantly affect energy dissipation in graphene nanoresonators [15]. These observations indicate that the transition from monolayer to bilayer graphene is not simply associated with an increase in structural thickness or stiffness; rather, it introduces additional mechanisms through which mechanical energy can be transferred and dissipated.

Interlayer shear and relative sliding are particularly relevant to this behavior. Liu et al. demonstrated that interlayer shear significantly modifies the vibration characteristics of multilayer graphene resonators [16], while Ye et al. showed that nanoscale roughness can contribute to damping during the oscillatory motion of bilayer graphene [17]. Direct investigations of graphene nanoelectromechanical resonators have further demonstrated the importance of interlayer friction as a source of mechanical dissipation [18,19]. The introduction of an additional graphene layer also modifies the underlying vibrational spectrum through interlayer coupling and the emergence of additional shear and out-of-plane modes, while influencing the behavior of flexural phonons [20]. Related atomistic investigations of the self-retracting motion of graphene flakes and graphene-based nanoscale oscillators

have illustrated how interfacial sliding and interlayer forces can drive complex mechanical energy exchange at graphene interfaces [21,22]. These mechanisms make AB-stacked bilayer graphene a particularly useful system for isolating the contribution of a single graphene–graphene interface to the overall dynamic response.

The relevance of graphene-related interfacial dissipation is not restricted to isolated nanoscale resonators. The ability of graphene interfaces to redistribute and dissipate mechanical energy has also motivated their exploitation in polymeric and fiber-reinforced composite materials. Graphene size and morphology have been shown to influence the damping response of graphene-containing polymer nanocomposites [23], while the incorporation of graphene nanoplatelets can substantially enhance the damping performance of polymers and composite structures [24]. Interfacial sliding of oriented multilayer graphene oxide has similarly been identified as an effective energy-dissipation mechanism in carbon-fiber-reinforced composites [25]. Atomistic simulations have provided additional evidence of the influence of graphene nanoplatelets on the dynamic response of polymeric nanocomposites [26], while graphene-based foam architectures [27] and graphene-nanoplatelet-modified hybrid composites [28] have also demonstrated enhanced damping characteristics. Although the length scales and surrounding material environments of these systems differ from those of pristine graphene nanoplates, these observations reinforce the broader significance of graphene interfaces as mechanisms for vibration-energy redistribution and dissipation.

MD simulation provides a particularly powerful framework for examining these phenomena because the atomic trajectories and interaction forces are explicitly resolved, allowing for lattice vibrations, anharmonic interactions, interlayer motion, and mechanical energy transfer to emerge from the atomistic description. The reliability of such predictions, however, depends strongly on the selected interatomic potential. Comparative MD studies have demonstrated that different carbon potentials can yield appreciable differences in the predicted phonon and thermal properties of graphene [29,30], while broader assessments of empirical potentials for carbon materials have emphasized that their accuracy can vary substantially depending on the structural, mechanical, or vibrational property under consideration [31]. Appropriate selection of the atomistic interaction model is therefore essential when investigating vibration and damping phenomena.

In a recent MD investigation, Giannopoulos and Iliopoulos examined the damping response of monolayer graphene subjected to localized harmonic out-of-plane excitation over a broad frequency range extending from 0.001 to 1 THz [32]. That study demonstrated a pronounced dependence of the dynamic response on excitation frequency, establishing frequency as an important governing parameter in atomistic graphene damping. Nevertheless, the investigation was restricted to monolayer graphene and therefore did not account for the additional energy-transfer mechanisms introduced by a graphene–graphene interface. Moreover, characterizing dissipation directly through the mechanical work performed during a complete loading cycle provides an alternative energy-based perspective that is particularly appropriate when the force–displacement response becomes nonlinear or hysteretic. More recent studies further demonstrate the continuing interest in the dynamic response and dissipation mechanisms of graphene resonators. At the atomistic level, molecular dynamics simulations have demonstrated that structural defects can modify the vibrational characteristics of graphene resonators [33]. Recent experimental work has shown that the energy dissipation and quality factor of graphene resonators can be strongly affected by their mechanical state and operating conditions [34], while recent simulations of multilayer graphene sheets have examined the dependence of natural frequencies and damping behavior on structural configuration [35]. Most recently, atomistic simulations of monolayer graphene nanodrums have revealed nonlinear resonance and damping behavior

dependent on excitation conditions [36]. Collectively, these studies show that the dynamic and dissipative response of graphene is sensitive to structural configuration, excitation conditions, and atomistic interactions. However, a direct comparison of monolayer and bilayer graphene under identical harmonic excitation, based on the mechanical energy dissipated over a complete force–displacement cycle, remains limited. This provides further motivation for the frequency-dependent atomistic analysis pursued here.

Large-scale atomistic calculations required for such analyses can be efficiently performed using the LAMMPS molecular dynamics platform [37]. In the present study, the atomic interactions are represented using the Reactive Force Field (ReaxFF), originally introduced by van Duin et al. [38]. ReaxFF employs a bond-order-dependent formulation in which atomic interactions evolve according to the instantaneous local environment rather than relying on a permanently prescribed bonding topology. The framework has subsequently been extended through several parameterizations for different carbon-containing systems. The ReaxFF description developed for RDX-based systems constituted an important stage in this development [39], while Srinivasan et al. introduced the C-2013 parameterization for condensed carbon phases, including graphene and other carbon allotropes [40]. Revised ReaxFF descriptions have also been evaluated for predicting the elastic and ultimate tensile properties of graphene, carbon nanotubes, diamond, and amorphous carbon [41].

Of particular relevance to the present investigation, Fthenakis et al. systematically evaluated the performance of several ReaxFF parameterizations for sp^2-carbon systems and proposed the GR-RDX-2021 potential [42]. The potential combines elements of the C-2013 and RDX parameterizations and introduces a dedicated description for graphene-type carbon environments. Its performance was assessed against structural, energetic, mechanical, strain-response, and phonon-related properties of graphene, together with additional tests involving carbon nanotubes and fullerenes [42]. The importance of specialized atomistic descriptions for graphene and other three-fold coordinated sp^2-carbon systems has also been demonstrated through graphene-oriented force-field development [43]. More generally, comparisons between empirical potentials and density functional theory calculations have shown that predicted graphene elastic properties can remain sensitive to the selected atomistic model [44]. Accordingly, the GR-RDX-2021 ReaxFF potential is adopted here as an atomistic description suitable for investigating the dynamic response of the considered graphene systems, while recognizing the inherent limitations associated with any empirical force-field representation.

Despite substantial progress in the characterization of graphene resonators, nonlinear damping, phonon-mediated losses, and interlayer friction, a direct atomistic comparison of the frequency-dependent mechanical energy dissipation of monolayer and AB-stacked bilayer graphene under identical harmonic excitation conditions remains comparatively limited. In particular, most previous investigations have characterized dissipation through quality factors, decay rates, phase relationships, or other effective damping measures. Less attention has been devoted to the direct evaluation of the net mechanical energy dissipated during a complete harmonic loading cycle from the reaction force–displacement hysteresis loop. Such an energy-based formulation is especially useful for nanoscale systems exhibiting nonlinear and frequency-dependent responses, since it does not require the atomistic system to be represented by an assumed phenomenological viscous damping coefficient.

The present study therefore investigates the frequency-dependent vibration damping and mechanical energy dissipation of monolayer and AB-stacked bilayer graphene using molecular dynamics simulations. Approximately square graphene nanoplates are subjected to localized harmonic out-of-plane excitation at their central region over a broad frequency range, while the corresponding vertical reaction force is directly obtained from the atomistic

simulations. Atomic interactions are described using the GR-RDX-2021 ReaxFF potential. The mechanical energy dissipated per excitation cycle is determined from the enclosed area of the resulting force–displacement hysteresis loop, and an energy-based equivalent damping ratio is subsequently employed to characterize the dissipative response. By comparing monolayer and bilayer graphene under otherwise identical excitation and boundary conditions, the investigation isolates the effect of introducing a single graphene–graphene interface and evaluates how its contribution evolves with excitation frequency. In this manner, the study establishes a direct connection between atomistic interlayer interactions, nonlinear vibration response, hysteretic energy dissipation, and effective damping, providing insight relevant to the response mitigation and dynamic design of graphene-based resonators and high-frequency NEMS.

Relative to our previous investigation of monolayer graphene [32], the present work introduces three main extensions: the inclusion of AB-stacked bilayer graphene and the associated interlayer coupling, the replacement of the previously employed AIREBO-M potential with the more recent GR-RDX-2021 ReaxFF parameterization, and, most importantly, an energy-based evaluation of the equivalent damping response instead of the force–displacement phase-lag approach employed previously. These extensions enable the influence of adding a second graphene layer and the associated interlayer interactions on the frequency-dependent damping response to be examined within a unified energy-based framework.

2. Interatomic Force Field and Atomistic Dynamic Formulation

The dynamic response of the graphene systems was described at the atomistic level using the Reactive Force Field (ReaxFF), originally introduced by van Duin et al. [38]. In contrast to conventional structural-dynamics formulations, in which restoring forces are commonly derived from an explicitly defined stiffness model and energy dissipation is introduced through viscous, hysteretic, or other phenomenological damping parameters, molecular dynamics (MD) determines the motion of individual atoms directly from the forces generated by the interatomic potential. Consequently, neither a macroscopic stiffness matrix nor a phenomenological damping coefficient is prescribed in the present atomistic model. Instead, the nonlinear force response and the redistribution of mechanical energy emerge from the collective dynamics of the atomic system.

ReaxFF is based on a bond-order formalism in which the interaction between neighboring atoms varies continuously with their instantaneous separation and local atomic environment [38]. The total bond order BO_{ij} between atoms i and j is expressed schematically as

$$BO_{ij} = BO_{ij}^{\sigma} + BO_{ij}^{\pi} + BO_{ij}^{\pi\pi}, \tag{1}$$

where BO_{ij}^{σ}, BO_{ij}^{π}, and $BO_{ij}^{\pi\pi}$ denote the contributions associated with the σ, first π, and second π bonding components, respectively. The subscripts i and j identify the interacting atoms. These bond-order contributions are continuous functions of the instantaneous interatomic distance r_{ij} between atoms i and j. Thus, changes in atomic positions during vibration continuously modify the local bond orders and, consequently, the potential-energy landscape of the system [38].

Within the standard ReaxFF formulation, the total potential energy of the atomic system E_{ReaxFF} can be written as follows [38]:

$$\begin{aligned} E_{\mathrm{ReaxFF}} = {} & E_{\mathrm{bond}} + E_{\mathrm{lp}} + E_{\mathrm{over}} + E_{\mathrm{under}} + E_{\mathrm{val}} + E_{\mathrm{pen}} + E_{\mathrm{coa}} \\ & + E_{\mathrm{tors}} + E_{\mathrm{conj}} + E_{\mathrm{Hbond}} + E_{\mathrm{vdW}} + E_{\mathrm{Coul}}, \end{aligned} \tag{2}$$

where E_{bond} is the bond-energy contribution; E_{lp} is the lone-pair energy; E_{over} and E_{under} account for over- and under-coordination, respectively; E_{val} is the valence-angle energy; E_{pen} is the valence-angle penalty contribution; E_{coa} represents the valence-angle conjugation energy; E_{tors} is the torsional energy; E_{conj} represents the torsional conjugation contribution; E_{Hbond} is the hydrogen-bond energy; and E_{vdW} and E_{Coul} denote the non-bonded van der Waals and Coulomb electrostatic energies, respectively. For the present systems, which consist exclusively of carbon atoms, terms associated specifically with hydrogen-containing environments do not contribute; nevertheless, they are retained in Equation (2) to present the general ReaxFF energy formulation. The individual energy contributions are functions of the instantaneous atomic configuration and, where applicable, the dynamically determined atomic charge distribution.

The resultant force $\mathbf{F}_i$ acting on atom i, is obtained from the gradient of the total potential energy,

$$\mathbf{F}_i = -\nabla_{\mathbf{r}_i} E_{\text{ReaxFF}}, \tag{3}$$

where $\mathbf{r}_i$ is the instantaneous position vector of atom i, and $\nabla_{\mathbf{r}_i}$ denotes the gradient operator with respect to the spatial coordinates of atom i.

The atomic trajectories are subsequently determined by integrating Newton's second law,

$$m_i \ddot{\mathbf{r}}_i = \mathbf{F}_i, \tag{4}$$

where m_i is the mass of atom i, and $\ddot{\mathbf{r}}_i$ is the acceleration vector of atom i. The double dot denotes the second derivative with respect to time. Accordingly, the instantaneous restoring behavior and nonlinear stiffness of the graphene structure emerge from the evolution of the interatomic forces rather than from a separately prescribed stiffness coefficient or stiffness matrix.

In the present study, the GR-RDX-2021 ReaxFF parameterization proposed by Fthenakis et al. [42] was employed, with graphene atoms represented by the graphene-specific carbon type C_g. Here, C_g denotes the carbon type introduced in GR-RDX-2021 for three-fold coordinated carbon atoms characteristic of graphene and related sp^2-carbon structures. GR-RDX-2021 combines the C-2013 description developed for condensed carbon phases [40] with interactions originating from the RDX-based ReaxFF framework [38,39]. The parameterization was assessed for several sp^2-carbon systems, including graphene, carbon nanotubes, and fullerenes, with its evaluation for graphene encompassing structural and energetic characteristics, mechanical response under deformation, and phonon dispersion [42]. This is particularly relevant to the present vibration analysis because both the restoring forces associated with graphene deformation and the evolution of its lattice-level dynamic response are governed by the same atomistic interaction model. Nevertheless, as with any empirical force field, the predicted response remains dependent on the adopted parameterization and should not be interpreted as an exact representation of every possible dynamic or interlayer phenomenon [31,42,44].

From a structural-dynamics perspective, the preceding atomistic formulation replaces an assumed macroscopic force–displacement law with forces obtained directly from the evolving many-body potential-energy surface. In the present simulations, a harmonic out-of-plane displacement is prescribed to the selected atoms in the central excitation region according to

$$u_z(t) = -A \sin(2\pi f t), \tag{5}$$

where $u_z(t)$ is the prescribed out-of-plane displacement at time t, A is the displacement amplitude, and f is the excitation frequency. The subscript z indicates the direction normal to the initial graphene plane, while the negative sign specifies that the excitation initially proceeds in the negative z-direction. As the prescribed displacement evolves, the atomic

configuration changes continuously and generates a corresponding time-dependent vertical reaction force, $F_z(t)$. In monolayer graphene, this response originates from the collective deformation and lattice dynamics of the covalently bonded carbon network. In bilayer graphene, additional mechanical energy transfer may arise from interactions and relative motion between the adjacent layers.

The reaction force–displacement response provides a direct energetic measure of the vibration behavior. Once a closed representative excitation cycle is obtained, the net mechanical energy associated with the hysteresis loop is evaluated as

$$\Delta E = \left| \oint F_z \, du_z \right|, \tag{6}$$

where ΔE is the net mechanical energy associated with the closed excitation cycle, F_z is the resultant reaction force in the out-of-plane z-direction acting on the prescribed excitation region, u_z is the corresponding imposed out-of-plane displacement, du_z is its differential increment, and the closed-integral symbol $\oint$ denotes integration over one complete closed force–displacement cycle. The absolute value is used so that the dissipated energy is reported as a positive quantity independently of the adopted force and displacement sign convention. Geometrically, ΔE corresponds to the area enclosed by the $F_z - u_z$ hysteresis loop.

Equation (6) establishes the principal connection between the atomistic simulation and the vibration-damping characterization adopted in this study. The interatomic potential determines the instantaneous forces, Newtonian dynamics governs the evolution of the atomic system, and the resulting reaction force under prescribed harmonic motion produces the force–displacement trajectory from which the cycle-dependent energy dissipation is obtained. Thus, the damping behavior is characterized energetically without introducing an artificial viscous damping coefficient at the atomistic level. This formulation is particularly appropriate for examining frequency-dependent and potentially nonlinear vibration responses and for assessing the additional energy-transfer mechanisms introduced by the graphene–graphene interface in the bilayer configuration.

3. Computational Model and Dynamic Excitation

MD simulations were performed using the LAMMPS simulation package [37] to investigate the frequency-dependent vibration response and mechanical energy dissipation of monolayer and bilayer graphene subjected to harmonic out-of-plane excitation. Two graphene configurations were considered: monolayer graphene and AB-stacked bilayer graphene. All systems were initially equilibrated at a temperature of 300 K to establish comparable thermal conditions prior to dynamic excitation.

The graphene nanoplates had in-plane dimensions of approximately 20 nm $\times$ 20 nm. In the bilayer configuration, the two graphene sheets were arranged according to AB (Bernal) stacking, with an initial interlayer separation of approximately 0.335 nm. To further assess the description of the interlayer interaction by the GR-RDX-2021 parameterization, an additional static interlayer-separation calculation was performed for AB-stacked bilayer graphene. The calculated energy–distance curve exhibited a well-defined minimum at an interlayer separation of approximately 0.330 nm, which is close to the equilibrium separation reported by first-principles benchmark calculations for AB-stacked bilayer graphene [45]. This value is also consistent with the initial interlayer separation of 0.335 nm adopted in the present simulations prior to equilibration. This validation primarily confirms the equilibrium interlayer distance predicted by the adopted parameterization and is not intended as a full quantitative assessment of the interlayer binding energetics. A sufficiently large vacuum region was introduced along the out-of-plane direction to prevent interactions between the graphene system and its periodic images. The computational models, stacking

configuration, boundary conditions, and excitation arrangement are illustrated in Figure 1. Prior to dynamic loading, the structures were subjected to an equilibration procedure to relax the atomic configuration and establish a stable state at the prescribed temperature.

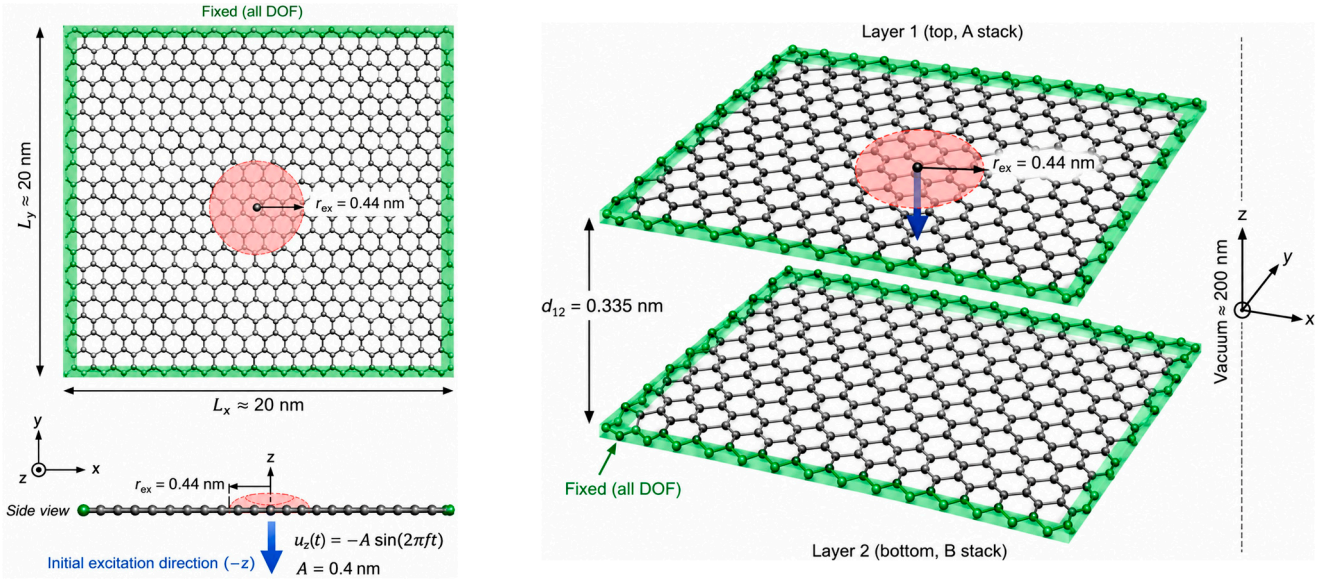

Figure 1. Computational models, boundary conditions, and excitation configuration considered in the MD simulations: (**a**) monolayer graphene and (**b**) AB-stacked bilayer graphene. The graphene nanoplates have in-plane dimensions of approximately 20 nm × 20 nm, with atoms along the perimeter fully constrained. A harmonic out-of-plane displacement with amplitude A = 0.4 nm is prescribed within a circular central excitation region of radius r_{ex} = 0.44 nm. In the bilayer model, the initial interlayer distance is d_{12} = 0.335 nm, and the excitation is applied exclusively to the upper graphene layer. The arrow indicates the initial excitation direction along the negative z-axis.

Following equilibration, fully constrained boundary conditions were imposed along the perimeter of each graphene nanoplate. Atoms located within approximately 0.14 nm from each edge were fixed in all translational degrees of freedom, thereby reproducing a fully clamped nanoplate. A circular region with a radius of r_{ex} = 0.44 nm was defined at the geometric center of the nanoplate as the excitation zone, where r_{ex} denotes the radius of the excitation region. For monolayer graphene, the prescribed motion was applied to the atoms contained within this central region. For bilayer graphene, excitation was applied exclusively to the corresponding central atoms of the upper graphene layer, while the lower layer was allowed to respond naturally through its interaction with the excited layer. To verify that the prescribed excitation does not lead to interlayer crossing at the low frequencies considered, an additional frame-by-frame analysis of the complete bilayer trajectories was performed. The minimum three-dimensional C–C distance between the two graphene layers was evaluated over 651 and 699 stored configurations at 0.001 and 0.01 THz, respectively. Minimum distances of 0.263 and 0.268 nm were obtained, confirming that the two layers remain distinct throughout the corresponding simulations despite the prescribed displacement amplitude of 0.4 nm.

The atoms within the excitation region followed the harmonic out-of-plane displacement prescribed by Equation (5). The negative sign in Equation (5) specifies that the excitation initially proceeds in the negative z-direction. Thus, in the bilayer configuration, the upper layer initially moves downward toward the underlying graphene layer before reversing its direction during the second part of the harmonic motion. The displacement amplitude was maintained at A = 0.4 nm for all simulations, while four excitation frequen-

cies, f = 0.001, 0.01, 0.1, and 1 THz, were investigated. The same excitation amplitude, excitation-region dimensions, and boundary conditions were maintained for the monolayer and bilayer systems to permit a direct assessment of the effects of excitation frequency and the presence of the second graphene layer on the dynamic response.

During the dynamic excitation stage, the unconstrained atoms that did not belong to the prescribed excitation region were integrated within the microcanonical (NVE) ensemble. No thermostat or barostat was applied during this stage, thereby preventing artificial energy exchange associated with temperature- or pressure-control algorithms. The atoms forming the constrained perimeter remained fixed, whereas the atoms within the excitation region followed the prescribed harmonic displacement. Accordingly, energy could be introduced into or removed from the atomistic system through the externally prescribed motion, while no additional phenomenological damping mechanism was imposed during the dynamic simulations.

At each simulation time step, the total vertical reaction force $F_z(t)$ associated with the excitation region was obtained from the vertical atomic force components of the prescribed atoms. Simultaneously, the out-of-plane displacement of the excitation region was recorded, allowing the corresponding reaction force–displacement trajectory to be constructed. The same procedure was applied to both graphene configurations and at each investigated excitation frequency.

The resulting force–displacement trajectories were used to construct the hysteresis loops employed for the energy-based damping analysis. For each closed representative excitation cycle, the mechanical energy dissipated per cycle was evaluated from the enclosed hysteresis-loop area according to Equation (6). This procedure provides a consistent basis for comparing the frequency-dependent energy dissipation of monolayer and bilayer graphene and, in particular, for assessing the additional contribution associated with the introduction of a single graphene–graphene interface.

4. Energy-Based Damping Calculation

The damping response was quantified using an energy-based approach based on the reaction force–displacement trajectories obtained from the MD simulations. No assumption of a linear force–displacement relationship was introduced. The prescribed displacement varies harmonically with time, while the corresponding reaction force reflects the instantaneous dynamic response of the atomistic system. Particularly at the higher excitation frequencies, this response may include appreciable inertial and lattice-dynamic contributions in addition to the restoring forces associated with structural deformation. Consequently, the resulting force–displacement trajectory is not expected, in general, to follow a linear path, and an energy-based formulation was adopted instead of introducing an equivalent linear stiffness or a phenomenological viscous damping coefficient.

The analysis interval was limited to $0 \leq t \leq 1.25T$, where $T = 1/f$ is the excitation period. This interval comprises the initial excitation stage from the equilibrium position to the first displacement extremum, followed by one complete harmonic displacement cycle. Starting from the equilibrium position at $t = 0$, the prescribed region moves in the negative z-direction and reaches the first displacement extremum, $u_z = -A$, at $t = 0.25T$. The mechanical work associated with this initial quarter-cycle was evaluated directly from the reaction force and prescribed displacement as

$$E_{0.25T} = \left| \int_0^{0.25T} F_z(t)\dot{u}_z(t)\,dt \right| = \left| \int_0^{-A} F_z\,du_z \right|. \quad (7)$$

Here, $E_{0.25T}$ represents the reference mechanical energy associated with the initial quarter-cycle. The first expression in Equation (7) evaluates the mechanical work from

the instantaneous reaction force and velocity of the prescribed excitation region, whereas the second represents the equivalent force–displacement integral between the equilibrium position and the first displacement extremum. The quantities F_z and u_z have been defined previously, while $\dot{u}_z$ denotes the velocity of the prescribed excitation region. Importantly, $E_{0.25T}$ is employed here as a reference energy obtained directly from the dynamic atomistic response and is not assumed to represent a purely elastic strain-energy quantity. This distinction is particularly relevant at the higher excitation frequencies, where the reaction force may contain appreciable inertial and lattice-dynamic contributions. The formulation therefore avoids the need to introduce an assumed equivalent stiffness.

Following the initial quarter-cycle, the prescribed displacement evolves through one complete closed cycle over the interval $0.25T \leq t \leq 1.25T$. During this interval, the displacement proceeds from $u_z = -A$, through the equilibrium position and the opposite displacement extremum, and subsequently returns to $u_z = -A$. The net mechanical energy associated with this closed excitation cycle was evaluated as

$$\Delta E = \left| \int_{0.25T}^{1.25T} F_z(t)\dot{u}_z(t)\,dt \right| = \left| \oint F_z\,du_z \right|. \tag{8}$$

The quantity ΔE corresponds geometrically to the area enclosed by the closed $F_z - u_z$ trajectory. The time-domain and force–displacement forms in Equation (8) are equivalent representations of the mechanical work accumulated over the complete excitation cycle. The absolute value is used so that ΔE is reported as a positive quantity independently of the adopted force and displacement sign convention. A narrow, nearly retraced force–displacement trajectory therefore corresponds to a comparatively small value of ΔE, whereas greater separation between the loading and unloading branches produces a larger enclosed area and, consequently, a larger cycle-dependent energy measure.

To permit comparison between systems exhibiting different reaction-force magnitudes and different reference energies, the cycle-dependent energy was normalized using the reference mechanical energy $E_{0.25T}$. An energy-based equivalent damping ratio was therefore defined as

$$\zeta_{\mathrm{eq}} = \frac{\Delta E}{4\pi E_{0.25T}} \tag{9}$$

Here, ζ_{eq} denotes the energy-based equivalent damping ratio. The form of Equation (9) follows the conventional energy-equivalent representation of damping, but the quantity obtained in the present study should not be interpreted as a phenomenological viscous damping coefficient prescribed in the equations of motion. Rather, ζ_{eq} provides a normalized measure derived directly from the atomistic reaction force–displacement response under the imposed harmonic excitation. Accordingly, it incorporates the frequency-dependent dynamic behavior represented by the MD simulations without requiring the force–displacement response to be linear or the underlying dissipation to be represented by a classical viscous-damping model.

The same calculation procedure and the same analysis interval were applied consistently to all four excitation frequencies and to both the monolayer and AB-stacked bilayer graphene configurations. Consequently, differences in ΔE and ζ_{eq} can be compared on a common energetic basis, allowing the effects of excitation frequency and the introduction of the second graphene layer on the effective damping response to be assessed directly.

5. Results and Discussion

5.1. Time-Domain Reaction Force Response

Figure 2 presents the time histories of the total vertical reaction force, F_z, for the monolayer and bilayer graphene nanoplates subjected to harmonic out-of-plane excitation. The results correspond to excitation frequencies of 1, 0.1, 0.01, and 0.001 THz, as shown in

Figure 2a–d, respectively. To facilitate comparison between simulations with substantially different oscillation periods, time is normalized with respect to the corresponding excitation period, T. The displayed interval extends from $t/T = 0$ to 1.25, comprising the initial quarter-cycle and the subsequent complete excitation cycle employed in the energy-based analysis.

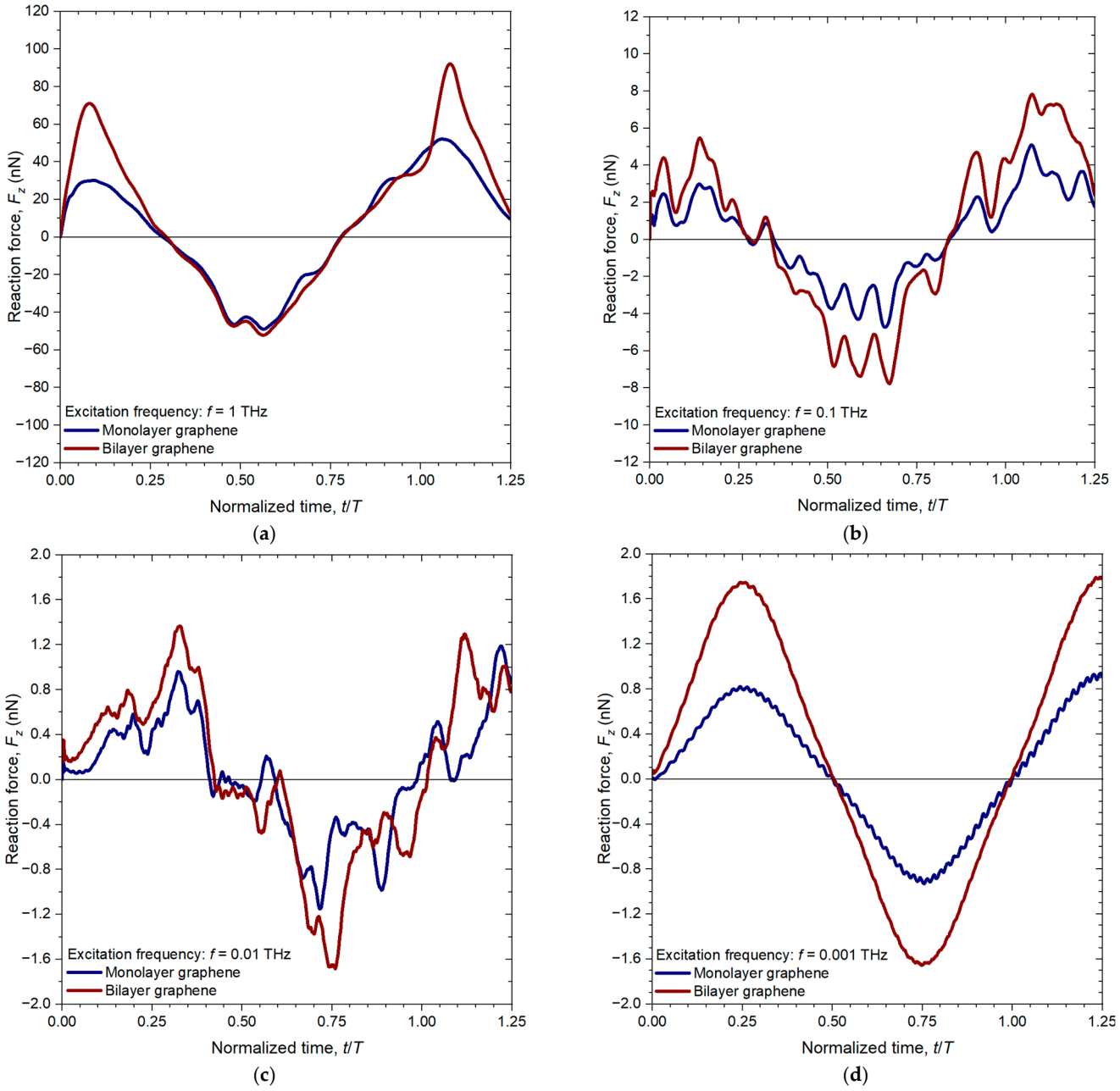

Figure 2. Time histories of the total vertical reaction force, F_z, for monolayer and AB-stacked bilayer graphene under harmonic out-of-plane excitation at frequencies of (**a**) 1 THz, (**b**) 0.1 THz, (**c**) 0.01 THz, and (**d**) 0.001 THz. Time is normalized with respect to the corresponding excitation period, T. The interval $0 \leq t/T \leq 1.25$ includes the initial quarter-cycle followed by the complete excitation cycle employed in the energy-based analysis.

The reaction-force response exhibits a pronounced dependence on excitation frequency, both in magnitude and waveform. At the lowest frequency of 0.001 THz [Figure 2d], the force histories are comparatively smooth and closely follow the overall periodic character of the imposed excitation. The bilayer develops a consistently larger force amplitude than the monolayer, while the overall shapes of the two responses remain similar. At

0.01 THz [Figure 2c], the reaction-force magnitude is lower and both configurations exhibit superimposed local oscillations. These fluctuations become more evident at 0.1 THz [Figure 2b], where the force response shows a more complex temporal evolution and the difference between the monolayer and bilayer becomes more pronounced over several portions of the excitation interval.

At the highest excitation frequency of 1 THz [Figure 2a], a substantially different force response is observed. Although the monolayer and bilayer histories remain relatively close over a considerable portion of the excitation interval, pronounced differences develop near the positive force maxima. In particular, the bilayer reaches markedly higher positive reaction forces during both the initial quarter-cycle and the final portion of the complete cycle, whereas the negative force response of the two configurations remains considerably closer. This asymmetric divergence indicates that the influence of the second graphene layer is not equivalent to a uniform scaling of the monolayer force response, but depends on the instantaneous stage and direction of the imposed motion.

The larger reaction-force amplitudes observed for the bilayer should be interpreted in the context of the prescribed-displacement excitation employed here. Under displacement-controlled harmonic excitation, the reaction force represents the dynamic force required to impose the specified motion and therefore reflects the combined effects of effective stiffness, inertia, and interlayer coupling. In the bilayer model, the prescribed displacement is applied only to the central atoms of the upper graphene layer, while the lower layer responds through interlayer interactions. Consequently, the measured reaction force also reflects the dynamic resistance associated with coupling to and mobilization of the second layer, and a larger force amplitude is therefore not inconsistent with the greater inertia of the bilayer. Moreover, because relative motion between the graphene layers is permitted, the bilayer cannot be interpreted simply as a conventional plate of doubled thickness.

Overall, Figure 2 demonstrates that the dynamic reaction-force response is governed by a non-monotonic interplay between excitation frequency and the presence of the second graphene layer. Moreover, the increasing complexity of the force histories at the intermediate and higher frequencies indicates that the instantaneous reaction force cannot be interpreted solely through the imposed displacement amplitude. The force histories alone, however, do not provide a direct measure of the mechanical energy associated with a complete excitation cycle. For this reason, the reaction force is subsequently examined together with the corresponding prescribed displacement through the force–displacement trajectories, allowing the cycle-dependent energy dissipation to be evaluated.

Figures 3 and 4 provide representative instantaneous configurations of the monolayer and AB-stacked bilayer graphene nanoplates, respectively, at four characteristic normalized time instants during the imposed harmonic motion. The snapshots correspond to t/T = 0.25, 0.50, 0.75, and 1.00 and are presented for all four investigated excitation frequencies. The same normalized time instants are used in each case, allowing the deformation patterns developed at different frequencies to be compared at equivalent stages of the prescribed excitation cycle. The accompanying side views provide a clearer representation of the out-of-plane deformation that is less readily distinguished from the perspective views alone.

For the monolayer graphene (Figure 3), the imposed localized excitation produces a deformation field concentrated around the central driven region and extending progressively over the surrounding sheet. Although the prescribed displacement amplitude is identical in all simulations, the instantaneous deformation patterns are not identical across the investigated frequencies. The differences become particularly apparent at the higher excitation frequencies, where more spatially localized features are visible around the excitation region and the deformation of the surrounding graphene sheet exhibits a

more complex profile. At the lower frequencies, the deformation appears comparatively smoother over the nanoplate.

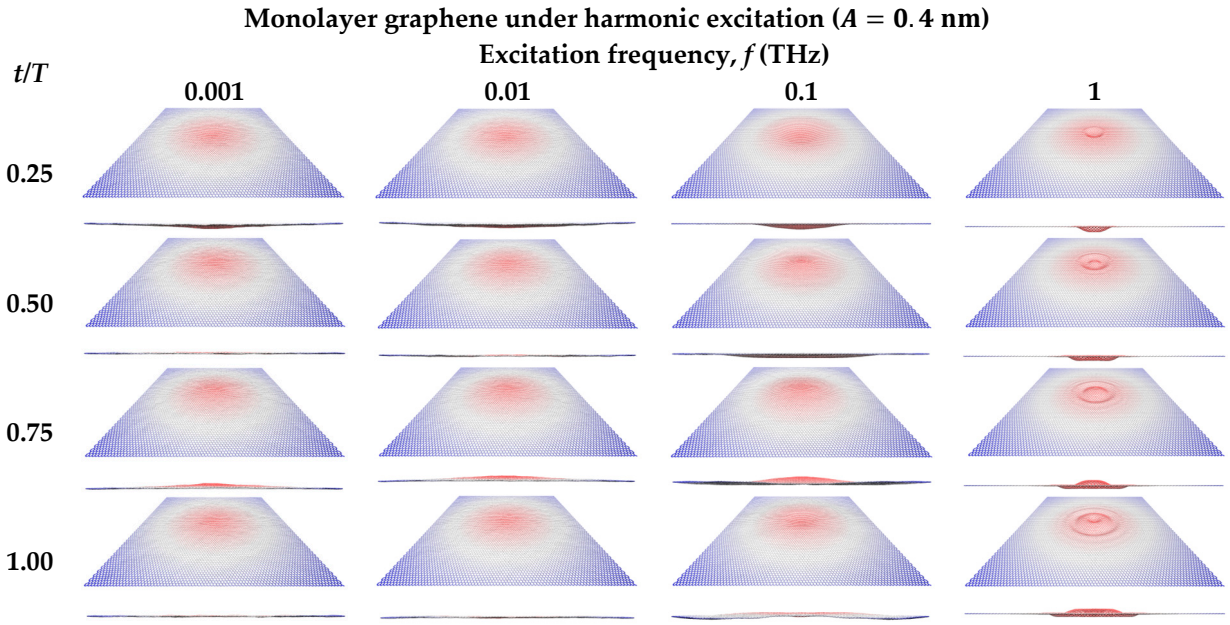

Figure 3. Instantaneous out-of-plane deformation of the monolayer graphene nanoplate at four normalized time instants (t/T = 0.25, 0.50, 0.75, and 1.00) for excitation frequencies ranging from 0.001 to 1 THz. For each condition, the upper image shows the overall deformation of the graphene sheet, while the lower image provides the corresponding side view to highlight the out-of-plane displacement. The harmonic excitation amplitude is A = 0.4 nm.

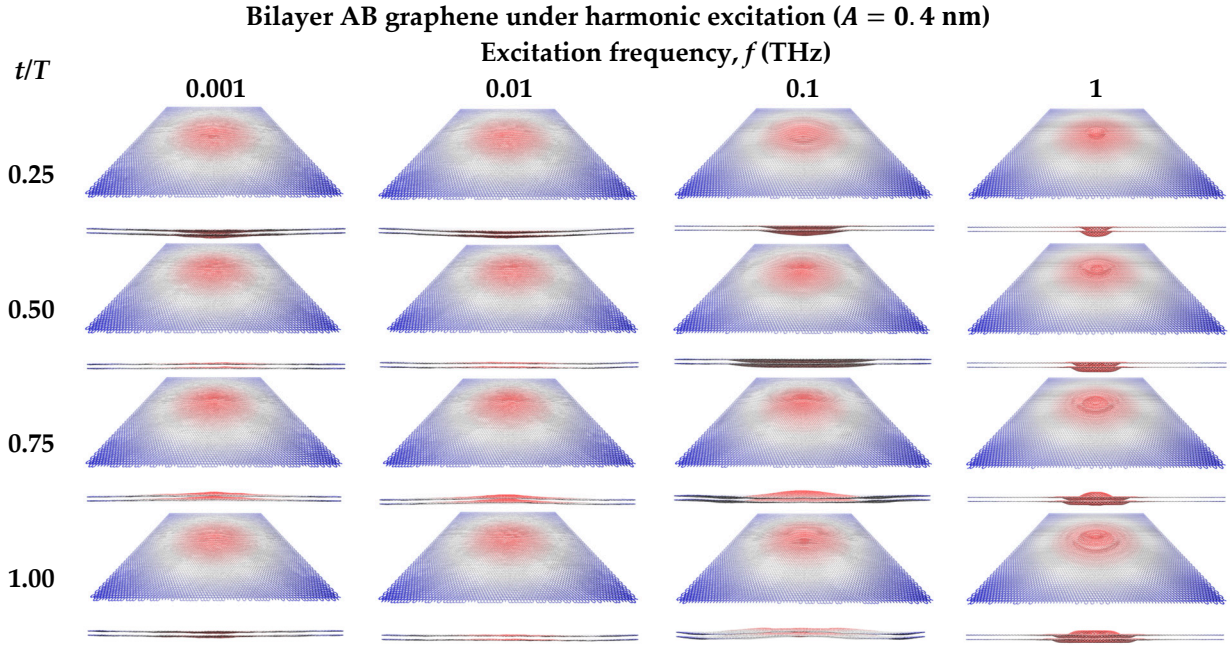

Figure 4. Instantaneous out-of-plane deformation of the AB-stacked bilayer graphene nanoplate at four normalized time instants (t/T = 0.25, 0.50, 0.75, and 1.00) for excitation frequencies ranging from 0.001 to 1 THz. For each condition, the upper image shows the overall deformation of the driven upper graphene layer, while the lower image provides the corresponding side view of the bilayer configuration, illustrating the deformation of both graphene layers. The harmonic excitation amplitude is A = 0.4 nm.

The corresponding bilayer configurations in Figure 4 show that the deformation is not confined to the directly excited upper layer. Although the harmonic displacement is prescribed exclusively to the central region of the upper graphene layer, motion is also evident in the lower layer, demonstrating the dynamic coupling between the two sheets through their interlayer interactions. The side views are particularly useful in this respect, as they reveal the simultaneous evolution of the two layers throughout the excitation cycle. As in the monolayer case, the spatial character of the deformation changes with excitation frequency, while differences between the two layers become more readily distinguishable at several stages of the cycle.

These instantaneous configurations provide a qualitative visualization of the frequency-dependent structural response but do not, by themselves, quantify the forces or the mechanical energy associated with the excitation. The corresponding reaction-force histories and force–displacement trajectories are therefore examined subsequently to determine how the observed dynamic response is reflected in the cycle-dependent energy dissipation.

5.2. Force–Displacement Hysteresis Response

Figure 5 presents the relationship between the vertical reaction force and the prescribed out-of-plane displacement for monolayer and AB-stacked bilayer graphene over one complete excitation cycle. The applied displacement is normalized by the excitation amplitude and expressed as $-u_z/A$. Accordingly, the cycle considered for the energy calculation begins at $t = 0.25T$, where $-u_z/A = 1$, and extends to $t = 1.25T$, returning to the same displacement state. The four panels correspond to excitation frequencies of 1, 0.1, 0.01, and 0.001 THz in Figure 5a–d, respectively.

A strong frequency dependence is evident in both the shape and the enclosed area of the force–displacement trajectories. At the lowest excitation frequency of 0.001 THz [Figure 5d], the trajectories are comparatively narrow and nearly single-valued over most of the displacement range. The bilayer develops larger reaction-force magnitudes than the monolayer, particularly toward the displacement extrema, but only a limited separation is observed between the successive branches of each trajectory. At 0.01 THz [Figure 5c], the response becomes more irregular, with local oscillations and a clearer separation between successive portions of the cycle. These features become substantially more pronounced at 0.1 THz [Figure 5b], where both configurations exhibit complex force–displacement paths and appreciably wider trajectories. The progressive loss of symmetry of the hysteresis loops with increasing excitation frequency can be associated with the transition from a nearly quasi-static response at low frequency to an increasingly dynamic response at higher frequencies. At 0.001 THz, the atomic structure has comparatively more time to accommodate the imposed displacement during each loading cycle, resulting in nearly symmetric loading and unloading trajectories. As the excitation frequency increases, atomic relaxation becomes increasingly unable to follow the imposed motion instantaneously, while inertial and phase-lag effects become more pronounced. The resulting nonequilibrium redistribution of atomic kinetic and potential energy contributes to the increasingly asymmetric force response. In the bilayer system, interlayer coupling provides an additional pathway for this frequency-dependent energy redistribution.

The increasingly complex and curved force–displacement trajectories also indicate that the dynamic response cannot be represented by a simple linear viscously damped system. At the atomistic scale, this behavior can be associated with the combined influence of nonlinear interatomic interactions and finite out-of-plane deformation, with additional complexity in the bilayer arising from interlayer coupling and relative motion between the graphene sheets. The present energy-based formulation captures the net cycle-dependent dissipation associated with this nonlinear response without assuming a phenomenological

damping law, although separation of the individual nonlinear mechanisms would require a dedicated nonlinear dynamic analysis.

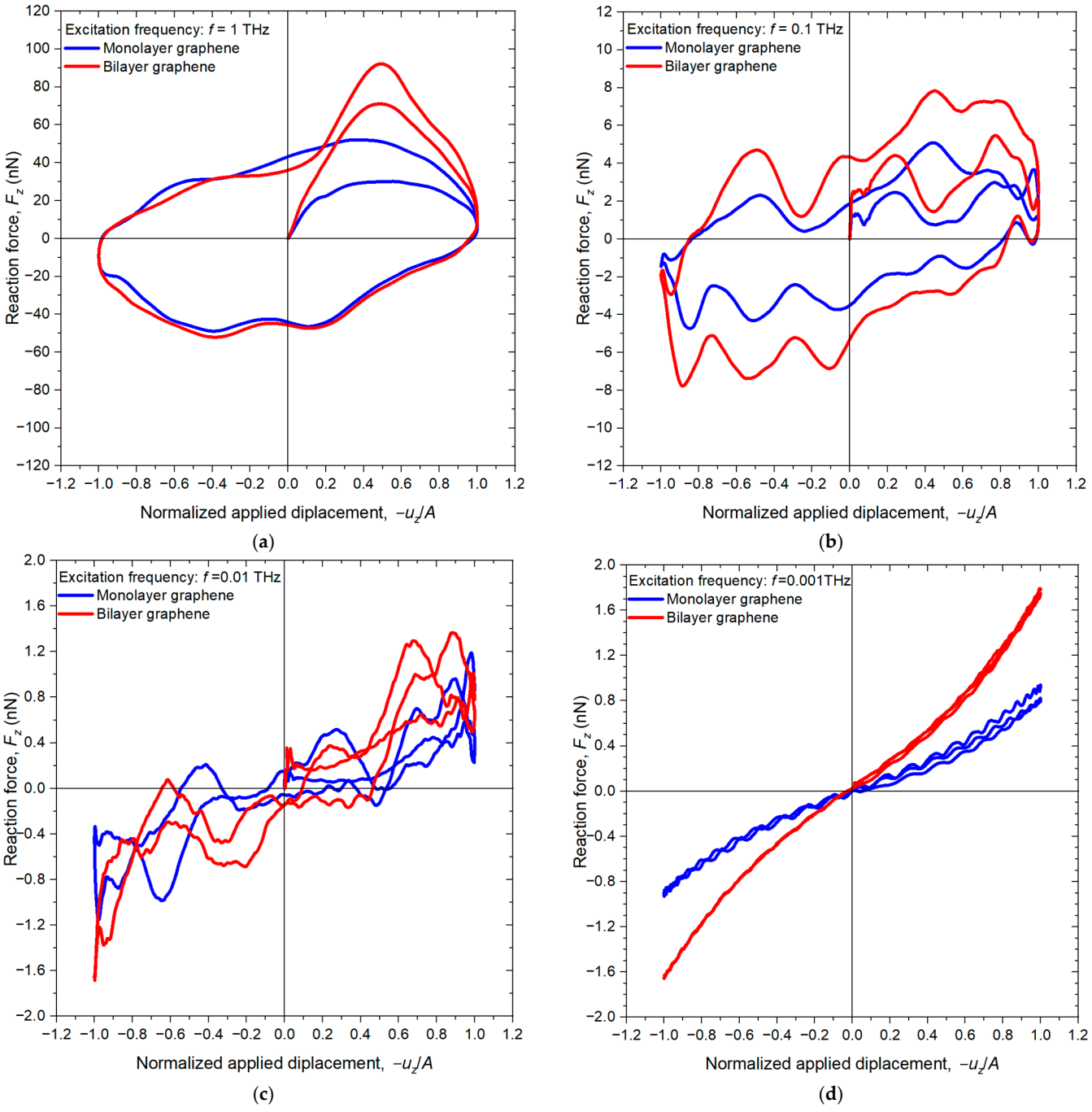

Figure 5. Reaction force–displacement trajectories of monolayer and AB-stacked bilayer graphene during one complete harmonic excitation cycle at frequencies of (**a**) 1 THz, (**b**) 0.1 THz, (**c**) 0.01 THz, and (**d**) 0.001 THz. The prescribed displacement is normalized by the excitation amplitude and expressed as $-u_z/A$. The trajectories correspond to the interval $0.25T \leq t \leq 1.25T$, and their enclosed areas provide the cycle-dependent mechanical energy, $\Delta E = |\oint F_z\, du_z|$, evaluated according to Equation (8).

The most pronounced hysteretic response occurs at 1 THz [Figure 5a]. Both graphene configurations form broad closed trajectories, although the bilayer exhibits a substantially larger upper branch over the positive-displacement region. In particular, while the monolayer reaches positive reaction forces of approximately 50 nN, the bilayer approaches 90 nN

over this portion of the cycle. By contrast, the negative-force branches of the two configurations remain considerably closer. The effect of the second graphene layer is therefore not equivalent to a uniform amplification of the monolayer response. Instead, the difference between the two configurations depends on the instantaneous stage and direction of the prescribed motion.

This behavior is particularly relevant to the adopted bilayer excitation configuration, in which the prescribed displacement is applied only to the central region of the upper graphene layer, while the lower layer responds through interlayer interactions. The resulting dynamic coupling modifies the reaction-force trajectory throughout the excitation cycle. Nevertheless, the force–displacement curves alone do not identify the individual atomistic mechanisms responsible for the observed differences, and the local oscillations and asymmetry of the trajectories are therefore interpreted here primarily as characteristics of the frequency-dependent dynamic response rather than being assigned to a specific dissipation mechanism.

Most importantly, Figure 5 demonstrates that peak reaction force alone is insufficient for characterizing the dissipative response. According to Equation (8), the mechanical energy associated with one complete excitation cycle, ΔE, is determined directly from the enclosed force–displacement trajectory, $\Delta E = |\oint F_z \, du_z|$. Consequently, both the progressive change in loop area with excitation frequency and the differences between the monolayer and bilayer trajectories provide the basis for the energy-based comparison presented in the following section.

5.3. Frequency-Dependent Energy Dissipation and Equivalent Damping

Figure 6 summarizes the frequency dependence of the equivalent damping ratio, ζ_{eq}, for the monolayer and AB-stacked bilayer graphene configurations. A pronounced frequency dependence is observed for both systems, while the effect of the second graphene layer varies considerably across the investigated frequency range.

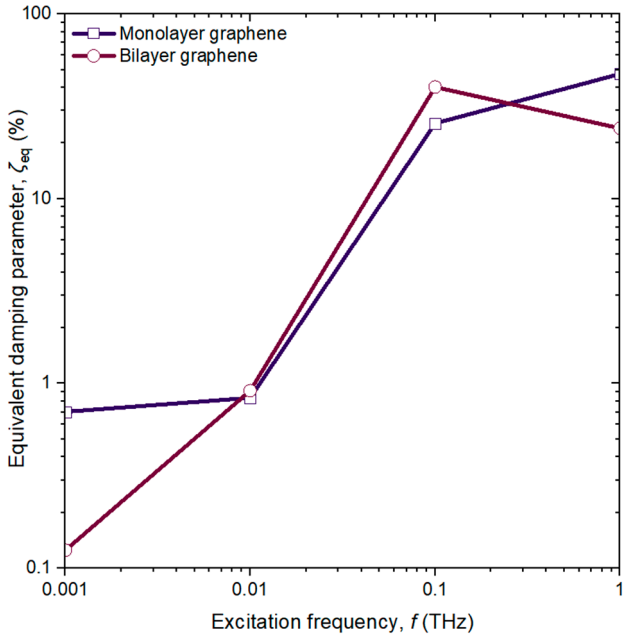

Figure 6. Frequency dependence of the equivalent damping ratio, ζ_{eq}, for monolayer and AB-stacked bilayer graphene under harmonic out-of-plane excitation.

At the lowest excitation frequencies, the equivalent damping remains comparatively small. For monolayer graphene, ζ_{eq} is approximately 0.70% at 0.001 THz and remains

at a similar level at 0.01 THz. The bilayer configuration exhibits a distinctly different low-frequency response. At 0.001 THz, its equivalent damping ratio is approximately 0.13%, substantially lower than that of the monolayer, whereas at 0.01 THz it increases to approximately 0.91%, slightly exceeding the corresponding monolayer value. Thus, even within the low-frequency range, the introduction of the second graphene layer does not produce a uniform increase or decrease in the normalized dissipative response.

A substantial increase in ζ_{eq} occurs as the excitation frequency increases to 0.1 THz. At this frequency, the equivalent damping ratios reach approximately 40% for both configurations, with the bilayer exhibiting a moderately higher value than the monolayer. This sharp increase is consistent with the considerably wider force–displacement trajectories observed at the higher excitation frequencies in Figure 5. Since ζ_{eq} is determined from the mechanical energy associated with the enclosed force–displacement trajectory relative to the reference energy defined in Equation (9), the increase cannot be attributed solely to the larger reaction-force amplitudes. Rather, it reflects the combined evolution of the force magnitude and the separation between successive branches of the dynamic force–displacement response.

At 1 THz, the two configurations exhibit a marked divergence, with the equivalent damping ratio reaching $\zeta_{eq}^{1L} = 47.4\%$ for the monolayer and $\zeta_{eq}^{2L} = 24.03\%$ for the bilayer. Examination of the corresponding energy quantities shows that $E_{0.25T}^{1L} \approx 1400$eV and $\Delta E^{1L} \approx 8339$ eV for the monolayer, whereas $E_{0.25T}^{2L} \approx 2800$eV and $\Delta E^{2L} \approx 8456$ eV for the bilayer. Thus, while the absolute cycle energy ΔE changes only slightly (approximately 1.4%), the reference energy $E_{0.25T}$ approximately doubles. Since the equivalent damping ratio is defined as $\zeta_{eq} = \Delta E/(4\pi E_{0.25T})$, the decrease in the bilayer damping ratio at 1 THz is primarily associated with the substantially larger reference energy entering the normalization, rather than with a reduction in the absolute cycle energy. Consequently, the lower normalized damping parameter of the bilayer should not be interpreted as lower absolute energy dissipation.

From a physical perspective, the non-monotonic bilayer response at 1 THz can be understood in terms of the additional interlayer coupling introduced by the second graphene sheet. Interlayer shear and coupled vibrational motion provide additional pathways for redistribution of the imposed vibrational energy between the two layers [15,16,20], thereby modifying the amplitude and phase of the reaction-force response rather than simply adding a dissipative contribution. Therefore, the effect of the second layer on the equivalent damping is inherently frequency-dependent, providing a plausible physical basis for the lower bilayer value observed at 1 THz.

The contrasting trends at the low- and high-frequency ends of Figure 6 further emphasize that the effect of the second graphene layer is frequency-dependent rather than additive. At low frequencies, interlayer coupling and relative motion provide additional pathways for energy redistribution, resulting in a stronger variation in the bilayer response than that of the monolayer. At the highest investigated frequency, the balance between reaction-force magnitude and cycle-dependent energy dissipation changes, leading instead to a reduction in the normalized bilayer damping parameter. Given the discrete frequency sampling, the connecting lines in Figure 6 are intended only as guides to the eye and should not be interpreted as evidence of strictly linear variation between the simulated frequencies.

The low-frequency behavior provides a further illustration of this distinction. At 0.001 THz, the bilayer develops larger reaction-force amplitudes than the monolayer but exhibits a substantially lower ζ_{eq}. This indicates that the presence of the second layer primarily increases the mechanical resistance to the imposed deformation under these slowly varying excitation conditions without producing a proportional increase in the net mechanical energy associated with the closed cycle. The response is therefore consistent with a comparatively more reversible coupled motion of the two graphene layers at the

lowest investigated frequency. The larger hysteresis-loop area of the bilayer indicates that the addition of a second graphene layer modifies the energy-dissipation process through interlayer coupling and the associated additional degrees of freedom. For three or more layers, additional interfaces would further modify the available energy-transfer pathways. However, this effect cannot be assumed to scale monotonically with the number of layers, since it also depends on excitation frequency and interlayer dynamics. A quantitative assessment of this dependence would require explicit multilayer simulations.

Overall, the results demonstrate that the influence of the second graphene layer on the energy-based damping response is strongly frequency-dependent and cannot be represented as a simple additive damping contribution. The transition from a reduced bilayer damping parameter at 0.001 THz, to comparable or moderately enhanced values at 0.01–0.1 THz, and finally to a substantially lower value at 1 THz indicates that interlayer coupling modifies the balance between reaction-force magnitude and cycle-dependent energy dissipation as the excitation frequency changes. Although the present force–displacement analysis does not resolve the individual atomistic mechanisms responsible for these variations, it demonstrates that layer number and excitation frequency are coupled parameters governing the effective dissipative response of graphene nanoplates.

The present energy-based damping estimates can be further assessed against previous computational and experimental studies. In our earlier molecular dynamics investigation of monolayer graphene [32], where damping was extracted from the phase lag between the imposed displacement and reaction force, the damping ratio increased from approximately 4×10^{-3} at 0.001 THz to values approaching 0.5 at 1 THz. The corresponding values obtained here from the force–displacement energy method are $\zeta_{eq} = 7.0 \times 10^{-3}$ and 0.474, respectively. Thus, despite the different force field and, more importantly, the different damping definition, the low-frequency predictions remain within the same order of magnitude, while the high-frequency results remain quantitatively comparable, providing useful cross-validation of the strong frequency dependence predicted by the present model. Independent studies also provide relevant order-of-magnitude benchmarks. Kunal and Aluru [12] reported $Q \approx 480$ for graphene nanoribbons at approximately 80 GHz, corresponding to $\zeta \approx 1/(2Q) \approx 1.0 \times 10^{-3}$, while room-temperature monolayer graphene resonators have exhibited Q values of the order of 10^2, corresponding to damping levels of approximately 5×10^{-3} [5,7]. These values are comparable in magnitude to the present low-frequency results. For multilayer graphene, Ferrari et al. [18] experimentally reported average quality factors of 53, 40, and 31 for monolayer, twisted-bilayer, and Bernal-stacked bilayer graphene, respectively, which correspond nominally to damping ratios of approximately 0.0094, 0.0125, and 0.0161 and demonstrate that the introduction of an additional graphene layer can substantially alter energy dissipation through interlayer interactions. Similarly, Lahiri et al. [14] observed a strong layer- and frequency-dependent damping response in multilayer graphene membranes under low-frequency cyclic loading, further supporting the view that multilayer damping cannot be described as a simple monotonic extension of the monolayer response. The considerably larger values predicted here at 0.1–1 THz should therefore not be interpreted as an intrinsic material damping constant, but as an equivalent energy-based measure of the strongly frequency-dependent response generated by the localized high-frequency excitation.

The present results were obtained for a fixed nanoplate size, excitation-region geometry, and prescribed displacement amplitude, which were maintained throughout the simulations to enable direct comparison between different layer configurations and excitation frequencies. Accordingly, the reported equivalent damping parameters should be interpreted as specific to the geometrical and loading conditions considered here, rather than as size- or amplitude-independent material properties. In addition, the present anal-

ysis is based on individual MD trajectories and does not constitute a statistical ensemble average. Systematic investigation of amplitude and size effects, together with statistical convergence over independent trajectories, therefore remains an important subject for future work. The present analysis considers four discrete excitation frequencies and was designed to characterize the frequency dependence of energy dissipation rather than to construct a resonance spectrum. Importantly, the excitation is displacement-controlled, with the central region following a prescribed harmonic motion of fixed amplitude. Consequently, proximity to resonance would not manifest as an amplification of the imposed displacement, as in a force-controlled response. The observed frequency dependence is therefore evaluated through the resulting reaction force–displacement response and associated cycle energy. Identification of individual resonance peaks would require a dedicated frequency-response or free-vibration analysis and is beyond the scope of the present study.

6. Conclusions

This study investigated the frequency-dependent vibration damping of monolayer and AB-stacked bilayer graphene using molecular dynamics and an energy-based approach derived from the reaction force–displacement hysteresis response. The results revealed comparatively low equivalent damping at 0.001–0.01 THz and a pronounced increase at 0.1–1 THz. For monolayer graphene, ζ_{eq} increased from approximately 0.7% at 0.001 THz to 47.4% at 1 THz.

The effect of the second graphene layer was strongly frequency-dependent. The bilayer exhibited lower equivalent damping than the monolayer at 0.001 THz, comparable or moderately higher values at 0.01–0.1 THz, and a substantially lower value at 1 THz. Importantly, larger reaction forces did not necessarily correspond to greater energy dissipation, demonstrating that the damping response is governed by the complete force–displacement trajectory rather than by force magnitude alone.

Overall, the results demonstrate that excitation frequency and interlayer coupling jointly govern the effective dissipative response of graphene. The proposed energy-based atomistic framework provides a direct means of identifying equivalent damping in a strongly frequency-dependent and nonlinear nanoscale system, offering fundamental insight for the modelling and potential tailoring of vibration mitigation in graphene-based resonators and NEMS.

Author Contributions: Conceptualization, A.V.I. and G.I.G.; methodology, A.V.I. and G.I.G.; software, A.V.I. and G.I.G.; validation, A.V.I. and G.I.G.; formal analysis, A.V.I. and G.I.G.; investigation, A.V.I. and G.I.G.; resources, G.I.G.; data curation, A.V.I. and G.I.G.; writing—original draft preparation, A.V.I. and G.I.G.; writing—review and editing, A.V.I. and G.I.G.; visualization, A.V.I. and G.I.G.; supervision, G.I.G.; project administration, G.I.G. All authors have read and agreed to the published version of the manuscript.

Funding: This research received no external funding.

Data Availability Statement: The data presented in this study are available on request from the corresponding author.

Conflicts of Interest: The authors declare no conflicts of interest.

References

1. Novoselov, K.S.; Geim, A.K.; Morozov, S.V.; Jiang, D.; Zhang, Y.; Dubonos, S.V.; Grigorieva, I.V.; Firsov, A.A. Electric field effect in atomically thin carbon films. *Science* **2004**, *306*, 666–669. [CrossRef] [PubMed]
2. Geim, A.K.; Novoselov, K.S. The rise of graphene. *Nat. Mater.* **2007**, *6*, 183–191. [CrossRef] [PubMed]
3. Lee, C.; Wei, X.; Kysar, J.W.; Hone, J. Measurement of the elastic properties and intrinsic strength of monolayer graphene. *Science* **2008**, *321*, 385–388. [CrossRef] [PubMed]

4. Bunch, J.S.; van der Zande, A.M.; Verbridge, S.S.; Frank, I.W.; Tanenbaum, D.M.; Parpia, J.M.; Craighead, H.G.; McEuen, P.L. Electromechanical resonators from graphene sheets. *Science* **2007**, *315*, 490–493. [CrossRef] [PubMed]
5. Chen, C.; Rosenblatt, S.; Bolotin, K.I.; Kalb, W.; Kim, P.; Kymissis, I.; Stormer, H.L.; Heinz, T.F.; Hone, J. Performance of monolayer graphene nanomechanical resonators with electrical readout. *Nat. Nanotechnol.* **2009**, *4*, 861–867. [CrossRef] [PubMed]
6. Hu, K.-M.; Bo, P.; Li, X.-Y.; Xin, Y.-H.; Bai, X.-R.; Li, L.; Zhang, W.-M. Resonant nano-electromechanical systems from 2D materials. *EPL* **2020**, *131*, 58001. [CrossRef]
7. Takamura, M.; Okamoto, H.; Furukawa, K.; Yamaguchi, H.; Hibino, H. Energy dissipation in edged and edgeless graphene mechanical resonators. *J. Appl. Phys.* **2014**, *116*, 064304. [CrossRef]
8. Takamura, M.; Okamoto, H.; Furukawa, K.; Yamaguchi, H.; Hibino, H. Energy dissipation in graphene mechanical resonators with and without free edges. *Micromachines* **2016**, *7*, 158. [CrossRef] [PubMed]
9. Eichler, A.; Moser, J.; Chaste, J.; Zdrojek, M.; Wilson-Rae, I.; Bachtold, A. Nonlinear damping in mechanical resonators made from carbon nanotubes and graphene. *Nat. Nanotechnol.* **2011**, *6*, 339–342. [CrossRef] [PubMed]
10. Croy, A.; Midtvedt, D.; Isacsson, A.; Kinaret, J.M. Nonlinear damping in graphene resonators. *Phys. Rev. B* **2012**, *86*, 235435. [CrossRef]
11. Keşkekler, A.; Shoshani, O.; Lee, M.; van der Zant, H.S.J.; Steeneken, P.G.; Alijani, F. Tuning nonlinear damping in graphene nanoresonators by parametric-direct internal resonance. *Nat. Commun.* **2021**, *12*, 1099. [CrossRef] [PubMed]
12. Kunal, K.; Aluru, N.R. Phonon-mediated loss in a graphene nanoribbon. *J. Appl. Phys.* **2013**, *114*, 084302. [CrossRef]
13. Jiang, J.-W.; Wang, J.-S. Graphene-based torsional resonator from molecular-dynamics simulation. *EPL* **2011**, *96*, 66007. [CrossRef]
14. Lahiri, D.; Das, S.; Choi, W.; Agarwal, A. Unfolding the damping behavior of multilayer graphene membrane in the low-frequency regime. *ACS Nano* **2012**, *6*, 3992–4000. [CrossRef] [PubMed]
15. Kim, S.Y.; Park, H.S. Multilayer friction and attachment effects on energy dissipation in graphene nanoresonators. *Appl. Phys. Lett.* **2009**, *94*, 101918. [CrossRef]
16. Liu, Y.; Xu, Z.; Zheng, Q. The interlayer shear effect on graphene multilayer resonators. *J. Mech. Phys. Solids* **2011**, *59*, 1613–1622. [CrossRef]
17. Ye, Z.; Otero-de-la-Roza, A.; Johnson, E.R.; Martini, A. The role of roughness-induced damping in the oscillatory motion of bilayer graphene. *Nanotechnology* **2014**, *25*, 425703. [CrossRef] [PubMed]
18. Ferrari, P.F.; Kim, S.; van der Zande, A.M. Dissipation from interlayer friction in graphene nanoelectromechanical resonators. *Nano Lett.* **2021**, *21*, 8058–8065. [CrossRef] [PubMed]
19. Ben-Shimon, Y.; Pradhan, A.; Ya'akobovitz, A. Material dissipation of graphene resonators. *Carbon* **2023**, *213*, 118185. [CrossRef]
20. Lindsay, L.; Broido, D.A.; Mingo, N. Flexural phonons and thermal transport in multilayer graphene and graphite. *Phys. Rev. B* **2011**, *83*, 235428. [CrossRef]
21. Popov, A.M.; Lebedeva, I.V.; Knizhnik, A.A.; Lozovik, Y.E.; Potapkin, B.V. Molecular dynamics simulation of the self-retracting motion of a graphene flake. *Phys. Rev. B* **2011**, *84*, 245437. [CrossRef]
22. Kang, J.W.; Lee, K.W. Molecular dynamics simulation of square graphene-nanoflake oscillator on graphene nanoribbon. *J. Nanosci. Nanotechnol.* **2014**, *14*, 9158–9164. [CrossRef] [PubMed]
23. Sarikaya, S.; Henry, T.C.; Naraghi, M. Graphene size and morphology: Peculiar effects on damping properties of polymer nanocomposites. *Exp. Mech.* **2020**, *60*, 753–762. [CrossRef]
24. Katsiropoulos, C.V.; Pappas, P.; Koutroumanis, N.; Kokkinos, A.; Galiotis, C. Enhancement of damping response in polymers and composites by the addition of graphene nanoplatelets. *Compos. Sci. Technol.* **2022**, *227*, 109562. [CrossRef]
25. Gong, L.; Zhang, F.; Peng, X.; Scarpa, F.; Huang, Z.; Tao, G.; Liu, H.-Y.; Zhou, H.; Zhou, H. Improving the damping properties of carbon fiber reinforced polymer composites by interfacial sliding of oriented multilayer graphene oxide. *Compos. Sci. Technol.* **2022**, *224*, 109309. [CrossRef]
26. Li, Z.; Li, T.; Zhang, K.; Wang, B. Dynamics responses of graphene nanoplatelets-reinforced polydimethylsiloxane nanocomposites: A molecular dynamics study. *Macromol. Theory Simul.* **2023**, *32*, 2300021. [CrossRef]
27. Li, T.; Du, J.; Xu, M.; Song, Z.; Ren, M. Lightweight and flexible graphene foam composite with improved damping properties. *Nanomaterials* **2022**, *12*, 1260. [CrossRef] [PubMed]
28. Erkliğ, A.; Younus, B.; Doğan, N.F.; Alsaadi, M.; Bulut, M.; Sulaiman, B.H. Vibration damping properties of graphene nanoplatelets filled glass/carbon fiber hybrid composites. *Int. Polym. Process.* **2023**, *38*, 145–153. [CrossRef]
29. Koukaras, E.N.; Kalosakas, G.; Galiotis, C.; Papagelis, K. Phonon properties of graphene derived from molecular dynamics simulations. *Sci. Rep.* **2015**, *5*, 12923. [CrossRef] [PubMed]
30. Zou, J.-H.; Ye, Z.-Q.; Cao, B.-Y. Phonon thermal properties of graphene from molecular dynamics using different potentials. *J. Chem. Phys.* **2016**, *145*, 134705. [CrossRef] [PubMed]
31. Qian, C.; McLean, B.; Hedman, D.; Ding, F. A comprehensive assessment of empirical potentials for carbon materials. *APL Mater.* **2021**, *9*, 061102. [CrossRef]

32. Giannopoulos, G.I.; Iliopoulos, A.V. Damping in monolayer graphene at high frequencies: Insights from molecular dynamics simulations. *Comput. Mater. Sci.* **2026**, *261*, 114276. [CrossRef]
33. Jiang, K.; Wang, J.; Yuan, J.; Wang, Q. Investigating vacancy-defect effects on the vibration characteristics of graphene resonators with molecular dynamics simulation. *Comput. Mater. Sci.* **2025**, *252*, 113794. [CrossRef]
34. Chen, D.-R.; Hu, I.-F.; Chin, H.-T.; Yao, Y.-C.; Raman, R.; Hofmann, M.; Liang, C.-T.; Hsieh, Y.-P. Ultrahigh-quality graphene resonators by liquid-based strain-engineering. *Nanoscale Horiz.* **2024**, *9*, 156–161. [CrossRef] [PubMed]
35. Yildiz, Y.O.; Sen, M.; Yigid, O.; Huseyinoglu, M.; Kara, S.E. Vibration analysis of variable-thickness multi-layered graphene sheets. *Appl. Sci.* **2025**, *15*, 9200. [CrossRef]
36. Varillas, J.; Kalbáč, M. Modulating the resonance response of monolayer graphene nanodrums. *Nanoscale* **2026**, *18*, 16582–16594. [CrossRef] [PubMed]
37. Thompson, A.P.; Aktulga, H.M.; Berger, R.; Bolintineanu, D.S.; Brown, W.M.; Crozier, P.S.; In 't Veld, P.J.; Kohlmeyer, A.; Moore, S.G.; Nguyen, T.D.; et al. LAMMPS—A flexible simulation tool for particle-based materials modeling at the atomic, meso, and continuum scales. *Comput. Phys. Commun.* **2022**, *271*, 108171. [CrossRef]
38. van Duin, A.C.T.; Dasgupta, S.; Lorant, F.; Goddard, W.A., III. ReaxFF: A reactive force field for hydrocarbons. *J. Phys. Chem. A* **2001**, *105*, 9396–9409. [CrossRef]
39. Strachan, A.; van Duin, A.C.T.; Chakraborty, D.; Dasgupta, S.; Goddard, W.A., III. Shock waves in high-energy materials: The initial chemical events in nitramine RDX. *Phys. Rev. Lett.* **2003**, *91*, 098301. [CrossRef] [PubMed]
40. Srinivasan, S.G.; van Duin, A.C.T.; Ganesh, P. Development of a ReaxFF potential for carbon condensed phases and its application to the thermal fragmentation of a large fullerene. *J. Phys. Chem. A* **2015**, *119*, 571–580. [CrossRef] [PubMed]
41. Jensen, B.D.; Wise, K.E.; Odegard, G.M. Simulation of the elastic and ultimate tensile properties of diamond, graphene, carbon nanotubes, and amorphous carbon using a revised ReaxFF parametrization. *J. Phys. Chem. A* **2015**, *119*, 9710–9721. [CrossRef] [PubMed]
42. Fthenakis, Z.G.; Petsalakis, I.D.; Tozzini, V.; Lathiotakis, N.N. Evaluating the performance of ReaxFF potentials for sp^2 carbon systems (graphene, carbon nanotubes, fullerenes) and a new ReaxFF potential. *Front. Chem.* **2022**, *10*, 951261. [CrossRef] [PubMed]
43. Fthenakis, Z.G.; Kalosakas, G.; Chatzidakis, G.D.; Galiotis, C.; Papagelis, K.; Lathiotakis, N.N. Atomistic potential for graphene and other sp^2 carbon systems. *Phys. Chem. Chem. Phys.* **2017**, *19*, 30925–30932. [CrossRef] [PubMed]
44. Lebedeva, I.V.; Minkin, A.S.; Popov, A.M.; Knizhnik, A.A. Elastic constants of graphene: Comparison of empirical potentials and DFT calculations. *Physica E Low.-Dimens. Syst. Nanostruct.* **2019**, *108*, 326–338. [CrossRef]
45. Mostaani, E.; Drummond, N.D.; Fal'ko, V.I. Quantum Monte Carlo calculation of the binding energy of bilayer graphene. *Phys. Rev. Lett.* **2015**, *115*, 115501. [CrossRef] [PubMed]

Disclaimer/Publisher's Note: The statements, opinions and data contained in all publications are solely those of the individual author(s) and contributor(s) and not of MDPI and/or the editor(s). MDPI and/or the editor(s) disclaim responsibility for any injury to people or property resulting from any ideas, methods, instructions or products referred to in the content.